Additive Manufacturing 35 (2020) 101383

Contents lists available at ScienceDirect

Additive Manufacturing

journal homepage: www.elsevier.com/locate/addma

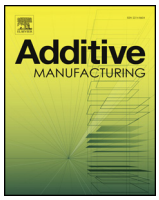

Research Paper

A meltpool prediction based scan strategy for powder bed fusion additive manufacturing

H. Yeung*, Z. Yang, L. Yan

National Institute of Standards and Technology, Gaithersburg, MD 20899, United States

ARTICLE INFO

Keywords:
Additive manufacturing
Scan strategies
Feedforward control
Machine learning

ABSTRACT

In this study a feedforward control method for laser powder bed fusion additive manufacturing is demonstrated. It minimizes the meltpool variation by updating the laser power based on a data-driven predictive meltpool model. A rectangular pattern is scanned multiple times on a customized LPBF testbed. The meltpool is monitored in situ by a high-speed camera, optically aligned with the heating laser. Constant laser power is applied for the first scan, and its meltpool images are used to train the model and adjust the laser power for the following scans. The meltpool images from these scans are compared, and a significant reduction in meltpool variation is achieved.

1. Introduction

Laser powder bed fusion (LPBF) is an additive manufacturing (AM) process in which a focused, high power laser selectively melts geometric patterns into layers of metal powder and builds near-net-shape parts layer by layer. The part quality is determined by many process parameters [1,2], such as the laser scan path, power, velocity, etc. For example, pores have been attributed to various phenomena related to the power-velocity attributes, such as keyhole collapse at high laser energy densities [3,4], or insufficient re-melting of adjacent scan vectors [5,6]. Moreover, Khairallah et al. also noted that turning the laser off at the end of a scan vector can potentially cause pores to be trapped under the rapidly solidified melt pool, and recommended laser power decrease at these locations [7]. A continuous scan strategy, which reduces such on and off was developed to reduce this end of scan porosity [8]. Apart from the solidification physics of a single scan, the general size, shape, and timing of a laser scanning pattern are also known to affect the local thermal history [9] and conductivity, resulting in inconsistent meltpool sizes.

Many earlier scan strategy studies have been focused on finding a single 'optimal' combination of laser power and velocity by determining the P–V (power-velocity) process map, paying little attention to this local variation in thermal properties due to conductivity or residual heat. Other studies have applied multi-physics simulation to capture these variations [10], but the computational cost limits its application to the scan strategy optimization. Machine learning-based simulation seems to provide the answer; multiple researchers [11–13] have demonstrated machine learning-based models with prediction accuracy close to the multi-physics simulation and computation time orders of magnitude less. However, we could not find any studies on applying these prediction models to optimize AM scan strategies. Further literature surveys show many machine learning studies on process monitoring and defect prediction [14,15]. Their potential applications on process control have also been suggested [16,17], but none was demonstrated experimentally. This could be due to the limitation of the experimental platform, such as the lack of continuous laser power adjustment capability within a scan vector.

In this study, we demonstrated a scan strategy optimization based on residual heat compensation. A neighboring-effect modeling (NBEM) method is built through a machine learning-based data-driven approach, and then used to tune the laser power for each digital scan position. The experiment was conducted on the Additive Manufacturing Metrology Testbed (AMMT) developed at the National Institute of Standards and Technology (NIST) [18,19]. Its open platform process control enabled a continuous laser power adjustment, which is fundamental for the implementation of advanced scan strategies.

2. AM process control and motnitoring

Fig. 1 shows the process control block diagram for the NIST AMMT. The AM Software handles slicing, path planning, digital interpolation and scan simulation (verification). The output files are (1) 2D layers described by vertices, (2) scan path described by modified G-codes (AM G-code) [9,11], and (3) time-stepped digital command of n x m

* Corresponding author.
E-mail address: ho.yeung@nist.gov (H. Yeung).

https://doi.org/10.1016/j.addma.2020.101383
Received 16 October 2019; Received in revised form 28 May 2020; Accepted 8 June 2020
Available online 12 June 2020
2214-8604/ Published by Elsevier B.V.

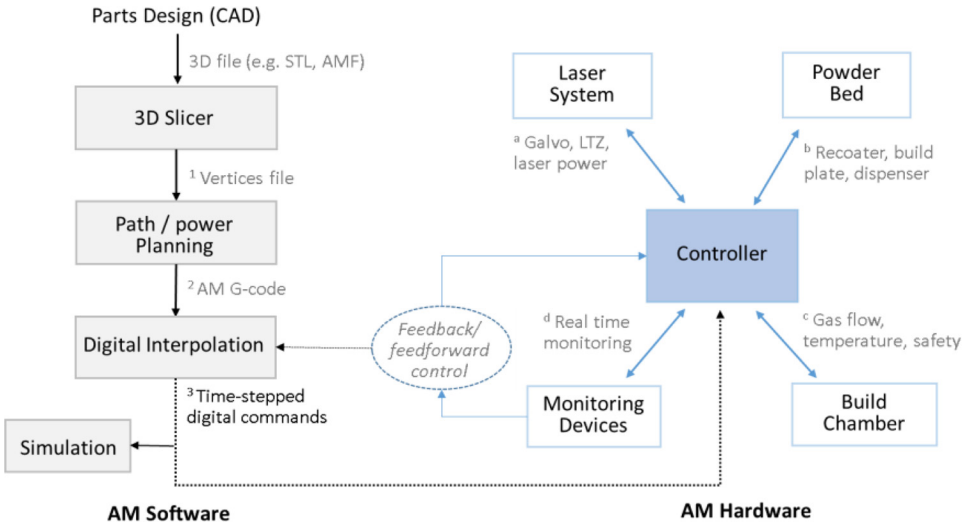

Fig. 1. AM process control block diagram.

numerical arrays; where n is the number of steps (per layer) and m is the number of control parameters. The time-stepped digital command can be first simulated or sent directly to the controller for execution. The AM controller controls hardware modules including (a) laser system, (b) powder bed, (c) build chamber and (d) monitoring devices. The monitoring signals can be used for feedback/feedforward controls and post-analysis.

2.1. Time-stepped digital command

The time-stepped digital command (also referred to as digital command) sent to the AM controller is created based on the xy2-100/sl2100 protocol [18], which updates x and y galvo positions at 100 kHz, or each 10 μs time-step. The digital command here expands the control parameters from two (x and y positions) to five, to include laser power (L), laser spot size (D), and triggers (T) for in-situ monitoring devices (Fig. 2a). The AM controller reads in the command array and executes one line every 10 μs (Fig. 2b). This ensures the synchronization between the laser position, power, spot size and in-situ monitoring devices (Fig. 2c). The digital command contains also scan speed (from the first derivative of x and y) and acceleration information (from the second derivative of x and y) since time is embed in the steps. Laser power (L) can be proportional to speed to obtain a constant power density scan strategy. It is also important that acceleration must be within the physical system's limit otherwise it will cause a following error (i.e., deviation from the commanded path) otherwise [8]. This digital command is the most accurate and complete way to describe the scan strategy, as the physical part is built solely based on it. For the same reason, optimization models can be built based on this digital command alone, and to adjust the L at each scan point to compensate the thermal/physical condition at that point.

2.2. Meltpool imaging and image analysis

During the laser powder bed fusion process, the meltpool is formed by laser beam irradiation on the metal powders, and then solidifies to the consolidated structure. Therefore, the meltpool is a primary feature of this process and its stability, dimensions and behavior determine to a great extent the quality and stability of the process [21,22]. The objective for controlling laser power during an AM build is to allow for more constant, unvarying meltpool size. A high-speed camera is set up coaxially [2] for in situ meltpool imaging (Fig. 2). The camera is triggered by the same digital commands for the laser position and power, hence the images can be mapped back to the exact scan positions (Fig. 2). The trigger intervals can be arbitrary as long as it is longer than the exposure time and multiple of one time-step (10 μs). Emitted light from the meltpool is filtered at 850 nm (40 nm bandwidth) and diverted by a dichroic mirror to the camera sensor with nominal 1:1 magnification and 8 μm/pixel size. The images were taken with 45 μs exposure time, 120-pixel x 120-pixel window, and 8-bit grayscale. The gray levels are used to relate to the meltpool temperatures [23], and for build quality prediction. This is demonstrated through the example below.

A spiral pattern was scanned on a bare stainless-steel (17 − 4) plate. Fig. 3a and b plot its speed and power. The nominal velocity is 1 m/s

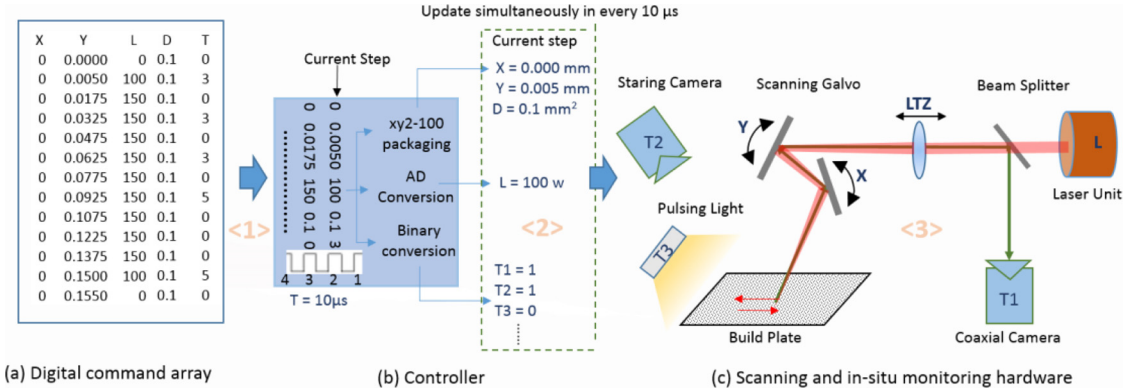

Fig. 2. Time-stepped digital commands and its execution. (a) A sample digital command array. (b) Controller reads the commands and executes it row by row, at 10 μs time-step. (c) Galvo, laser power, laser diameter, and in-situ monitoring devices status are updated at every 10 μs. Cameras are triggered by T.

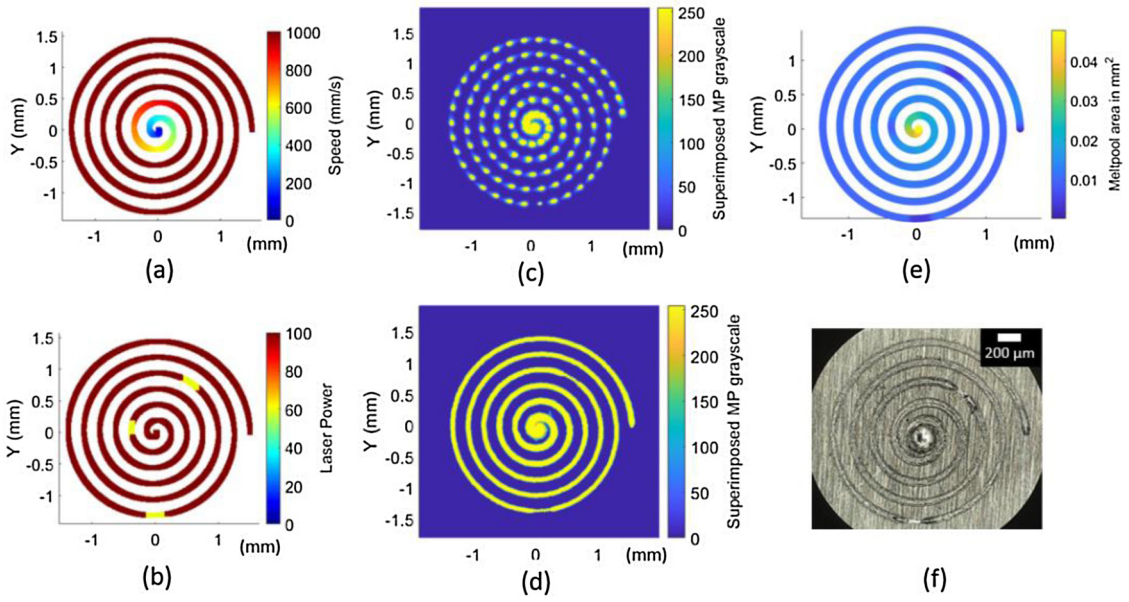

Fig. 3. Meltpool image analysis example. (a) Laser speed (b) Laser power. (c) Virtual build plate with equivalent frames per second = 4 kHz. (d) Continuous track created from meltpool images. (e) Meltpool area plot against its location. (f) Microscopic image of the physical scan tracks.

but is slowed down when approaching to the center to keep the acceleration within the system limits. The nominal power is 100 W but is lowered to 60 W for 300 µs at three different locations (yellow color in Fig. 3b), to create changes in the meltpool. A 'virtual build plate' is created by a bitmap of the same dimension as the scan area (3 mm x 3 mm) and the same pixel resolution (8 µm/pixel) as the meltpool image (Fig. 3c). The meltpool images are then 'superimposed' to the positions they were taken, by taking the maximum grayscale level among them. If the frame rate is high enough, a continuous 'virtual' scan track will form as shown in Fig. 3d. Fig. 3e plots the meltpool image area by color for direct visualization of the meltpool size variation. Comparing the virtual (Fig. 3d) and physical scan tracks (Fig. 3f), the variations of meltpool size at the lower laser power and at the center of the spiral are faithfully recorded by the meltpool images. The contour with the grayscale intensity level of 80 is found to best match the physical meltpool width, it is used to infer melt pool boundary from the high-speed images and calculate meltpool image dimensions.

The 'virtual build plate' (meltpool intensity and area plots in Fig. 3d and e) were originally developed to predict the potential lack of fusion and keyholing defects. They were provided here as a demonstration of continuous laser power control and accurate in-situ meltpool monitoring capabilities. The close correlation between the lack of fusion locations on the physical plate (Fig. 3f) and the virtual plate (Fig. 3d) implies that if the lack of fusion defects are eliminated on the virtual plate by keeping a constant meltpool, the lack of fusion defects could also be eliminated on the physical plate. Three potential lack of fusion defects were seeded by lowering the laser power to 60 W (the yellow regions in Fig. 3b), but only two can be observed on the virtual / physical plate (Fig. 3d and f). This implies a lower laser power does not necessarily result a smaller meltpool or a lack of fusion defect. When the scan approaching the center, the center region is heated up and same laser power level can create a larger meltpool. The objective of this study is only to keep a constant meltpool area, but it is believed that a more constant meltpool will give a better part quality.

3. Modeling and optimization methods

This section introduces the fundamental approaches of modeling and optimization methodologies used in this study for scan strategy improvement. It uses the building time, laser power, scan speed, and neighboring effect factors (Eq. 1) as input variables for the meltpool size predictive model. However, the scan strategy optimization uses the laser power as the single design variable to reduce the meltpool variation. A data-driven model predicting meltpool image size is developed based on the data collected from the original experiment. The optimizer iteratively updates the laser power (L column in Fig. 2a) in the scan commands to keep the meltpool size more constant. A series of experiments were designed to verify the modeling and optimization work.

The modeling method in this study builds upon the authors' previous work named Neighboring Effect Modeling Method (NBEM) [24]. The fundamental theory of the NBEM method is that the meltpool size depends on, in additional to laser power and scan speed, the thermal history of the scanning process. Eq. (1) shows the formulation of meltpool size S_i for scan point i, and the related variables laser power P_i, scan speed v_i, and neighboring effect factors $\theta_i^{\Delta t}$ and $\theta_i^{\Delta d}$. The last two factors represent the cumulative effect of all neighboring points to the current point i based on time difference Δt and spatial difference Δd.

$$S_i = f(P_i,\ v_i,\ \theta_i^{\Delta t},\ \theta_i^{\Delta d}) \tag{1}$$

Under this theory, the NBEM factors summarize the influence of the previous energy density of all neighboring points according to the cooling rates. The magnitude of these factors depends on the part geometry and laser scan path. The geometry of the part determines the quantity of neighboring points. The scan path determines how the neighboring points relate to the current point. For example, two points may be spatially close to one another but the scan path might be such that a long time exists between when the laser spot hits each point [24]. Considering the cooling rate, spatially closer points with long traveling time cannot provide sufficient influence on the current melting point. This study modifies the original formulation to a new form by adding the global building time factor and removing the low sensitive spatial NBEM factor to improve predictive accuracy. The formulation of NBEM model used in this study is:

$$S_i = f(t_i,\ P_i,\ v_i,\ \theta_i^{\Delta t}) \tag{2}$$

where variable t_i represents the global building time at current scanning point i. $\theta_i^{\Delta t}$, the summation the neighboring effect from time perspective, can be presented as:

Table 1
Polynomial coefficients and terms of Eq. (2) used in this study.

Coefficient	Term	Coefficient	Term	Coefficient	Term	Coefficient	Term
c_0	Intercept	c_5	x_1x_2	c_{10}	x_3x_4	c_{15}	$x_2x_3x_4$
c_1	x_1	c_6	x_1x_3	c_{11}	x_4^2	c_{16}	$x_1x_4^2$
c_2	x_2	c_7	x_2x_3	c_{12}	$x_1x_2x_3$	c_{17}	$x_2x_4^2$
c_3	x_3	c_8	x_1x_4	c_{13}	$x_1x_2x_4$	c_{18}	$x_3x_4^2$
c_4	x_4	c_9	x_2x_4	c_{14}	$x_1x_3x_4$	c_{19}	x_4^3

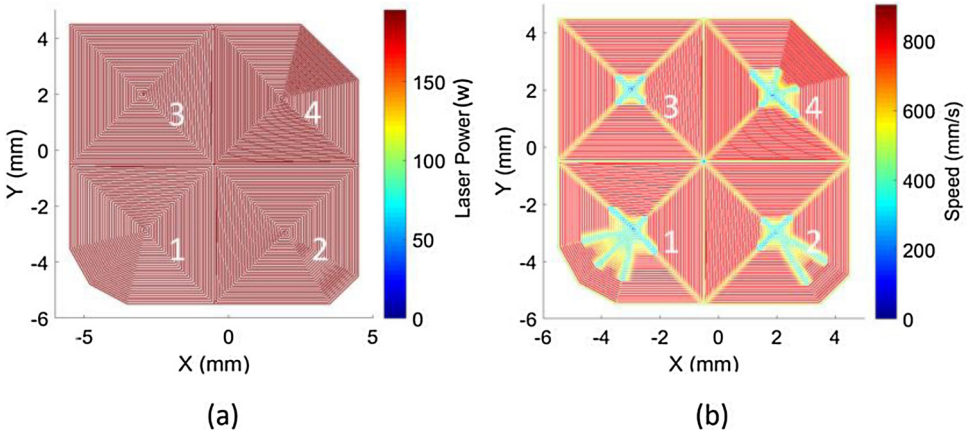

Fig. 4. Scan strategy for the first experiments. Numbers indicate the scanning sequence. (a) Laser power. (b) Laser speed.

Table 2
Experiment design.

Scenario	Constraint of Power (W)		Objective Meltpool Area (mm^2)	
	Lower Bound	Upper Bound	Lower Bound	Upper Bound
1	100	195	0.014	0.026
2	100	195	0.016	0.024
3	100	195	0.018	0.022
4	50	250	0.014	0.026
5	50	250	0.016	0.024
6	50	250	0.018	0.022

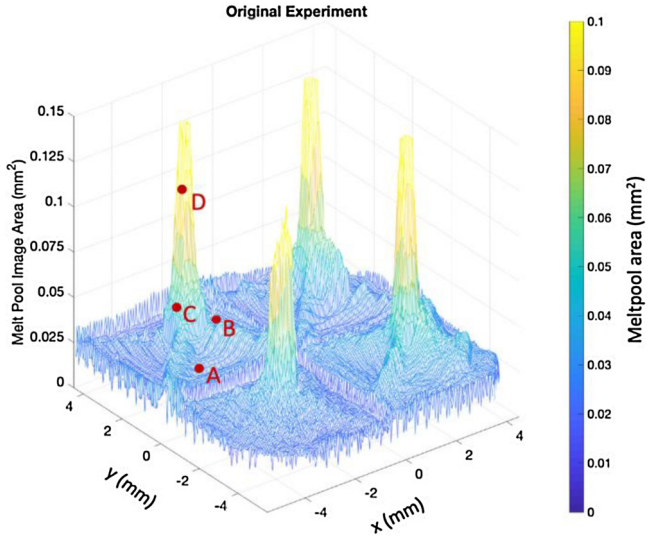

Fig. 5. 3D plot of the meltpool area for the original experiment. Meltpool images at locations marked by A - D are plotted in Fig. 6.

$$\theta_i^{\Delta t} = \sum_{j=1}^{n} f_t(\Delta t_{ij}) \frac{P_{ij}}{v_{ij}} \tag{3}$$

where Δt_{ij} is the travel time from point j to point i along the laser scan path. P_{ij} and v_{ij} are the laser power and scan speed of point j in the neighboring zone of the current point i. The effect for point j is:

$$f_t(\Delta t_{ij}) = a_1 e^{a_2 \Delta t_{ij}} \tag{4}$$

where $f_t(0) = 1$ and $f_t(\infty) = 0$. The parameters a_1, a_2 can be derived from data-driven approach based on the experiments. In this study, Δt_{max} is set to 300 000 μs that represents the maximum time difference in the NBEM model. The estimated $a_1 = 1$, $a_2 = -0.00001029$ were used, as well as an order of '1113' for the polynomial variables t_i, P_i, v_i, and $\theta_i^{\Delta t}$ in Eq. (2). Table 1 lists the coefficients and terms of the polynomial model, where $x_1 = t_i$, $x_2 = P_i$, $x_3 = v$, and $x_4 = \theta_i^{\Delta t}$.

The purposes of the scan strategy optimization are meltpool size control and variation reduction. To achieve these goals, the potential design variables for optimization can be laser power, scan speed, and laser scan path. Modifying scan speed or laser scan path requests the significant changes in scan commands, therefore laser power is selected as the single design variable for the optimization, which focuses on managing the meltpool size into the desired range. Steps in the optimization algorithm are:

Step 1. Compute the NBEM variables t_i, P_i, v_i, and $\theta_i^{\Delta t}$ from the scan commands x, y, and L columns, of each time step i.

Step 2. Compute the meltpool area of each time step using by NBEM model for current scan strategy

Step 3. Locate the irregular sized meltpool from the estimation $S_h > S_{max}$ and $S_l < S_{min}$. Subscripts h and l represent the index of the time step when larger and smaller meltpool may appear due to the scan strategy. S_{max} and S_{min} are the boundaries of desired meltpool range.

Step 4. For all irregular meltpool, $P_h^{k+1} = P_h^k*(1 - m\Delta p)$ for oversized meltpool and $P_l^{k+1} = P_l^k*(1 + m\Delta p)$ for undersized meltpool, where P_h^{k+1} and P_l^{k+1} are the updated laser power for h and l at $k+1$ iteration, Δp is the portion of laser power adjustment, and m is the decrement coefficient of each iteration. In this study Δp is set to 10 %, m is set to $\frac{10}{9+k}$.

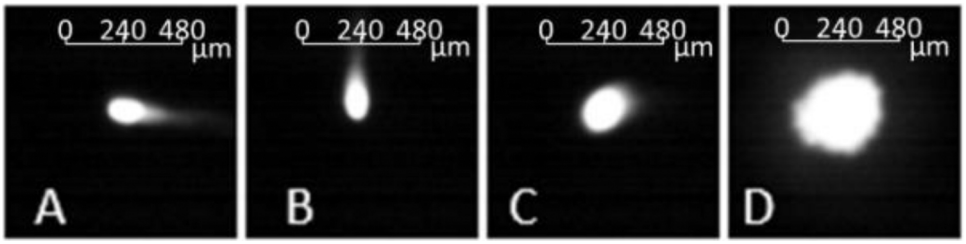

Fig. 6. Example meltpool images for the original experiment.

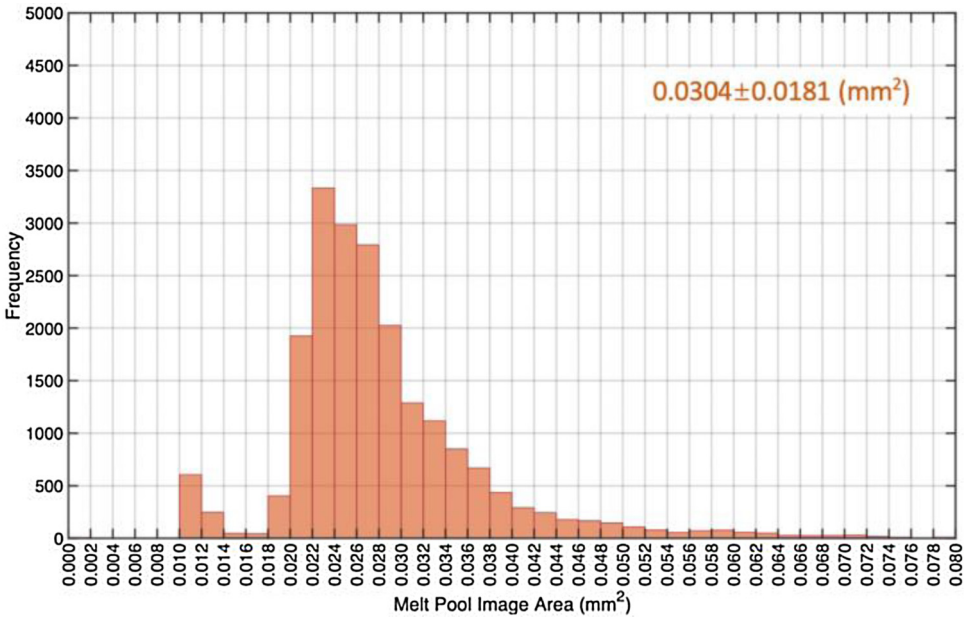

Fig. 7. Histogram of the melt pool image area for the original experiment.

Table 3
Coefficients of NBEM model.

	10^{-6}		10^{-6}		10^{-6}		10^{-6}
c_0	0	c_5	0	c_{10}	0.2450	c_{15}	0.0005
c_1	−0.0039	c_6	0	c_{11}	−0.0038	c_{16}	0
c_2	136.9875	c_7	−0.0414	c_{12}	0	c_{17}	0.0079
c_3	−2.3710	c_8	0	c_{13}	0	c_{18}	−0.0024
c_4	0	c_9	−1.1516	c_{14}	0	c_{19}	0.0038

Step 5. Compute the meltpool area of each time step using the new scan strategy with updated laser power.

Step 6. Calculate $\Delta h = \frac{\mu_h^{k+1} - \mu_h^k}{\mu_h^k}$ and $\Delta l = \frac{\mu_l^{k+1} - \mu_l^k}{\mu_l^k}$. μ_h^i and μ_l^i represent the total number of large and small meltpools for the k^{th} iteration. If both Δh and Δl converge, the current scan strategy is considered optimal. Otherwise, set the new m and then return to Step 3.

Seven experiments (scans) were conducted, all with the same concentric spiral-in pattern and scan speed as shown in Fig. 4a. The scan is divided into 4 islands, the number on each island indicates the scanning order. The nominal scan speed is set to 800 mm/s and is reduced during turns. Fig. 4b, however, shows the laser power for the first experiment only. Two constant laser power levels applied, 100 W for the contour (perimeter of the pattern) and 195 W for the infills. The laser spot size is set to 85 µm. The scan strategy and meltpool images for the first experiment, also referred to as the original experiment, are used to build the NBEM model.

The other six experiments were designed to validate the optimal scan strategy according to the constraint of power and the objective meltpool image area. As shown in Table 2, Scenarios 1–3 set the laser power from 100 W to 195 W. The target meltpool image area of Scenario 1 ranged from 0.014 mm^2 to 0.026 mm^2 and gradually narrowed to 0.018 mm^2 to 0.022 mm^2 for Scenario 3. Scenarios 4–6 have the same target meltpool area range, but the boundary condition of laser power extends to 50 W to 250 W. All scenarios have the same target for the mean meltpool area, 0.02 mm^2.

4. Experiment results and discussion

Fig. 5 shows the 3D plot of the measured meltpool image area for the original experiment using the scan strategy shown in Fig. 4. The meltpool images located near the center of each island have a significantly larger area than the average. Fig. 6 shows the actual meltpool images taken by the coaxial camera at locations A–D marked in Fig. 5. A total of 20,902 meltpool images were collected for each experiment. Fig. 7 plots the histogram of the meltpool image areas measured. The average is 0.0304 mm^2 with a standard deviation of 0.0181 mm^2.

The model is fitted by the polynomial regression method using Eq. (1) and Eq. (2), with the data from the original experiment. To test the predictive accuracy, the model is built by 50 % of the data and tested by the remaining 50 %. The formulation of The Average Relative Error Magnitude (AREM) [25] is shown in Eq. (5), where y_i is the observed meltpool image area from the experiment, $\hat{y}_i$ is the estimated area from the model, and n is the total data points. The data used to build the model includes only effective laser power (P > 0); the meltpool images with area = 0 are thus eliminated from the training and testing datasets. AREM of the model from Eq. (1) is 23 % and the model from Eq. (2) is 17 %. The model with the lower predictive error is implemented. The values of the fitted coefficients for Eq. (2) are shown in Table 3. The

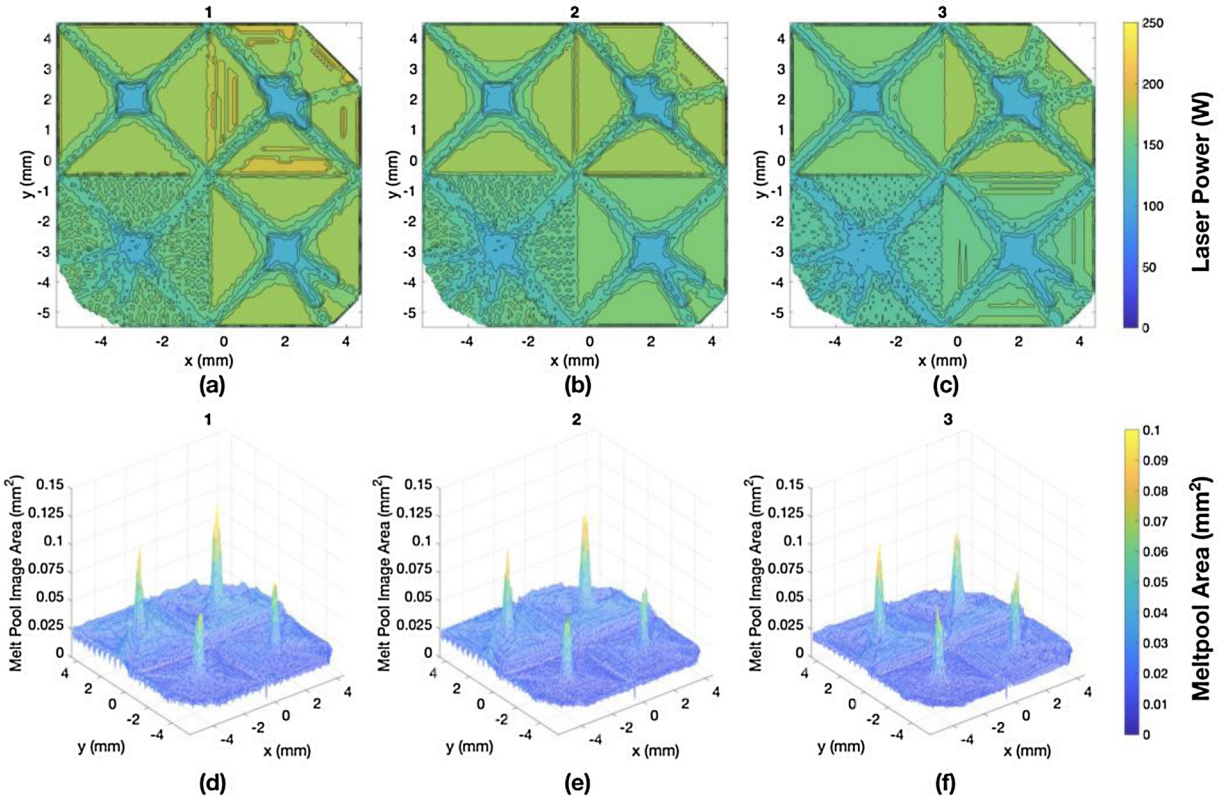

Fig. 8. Optimized laser power (a – c) and meltpool image area (d – f) for Scenarios 1 to 3.

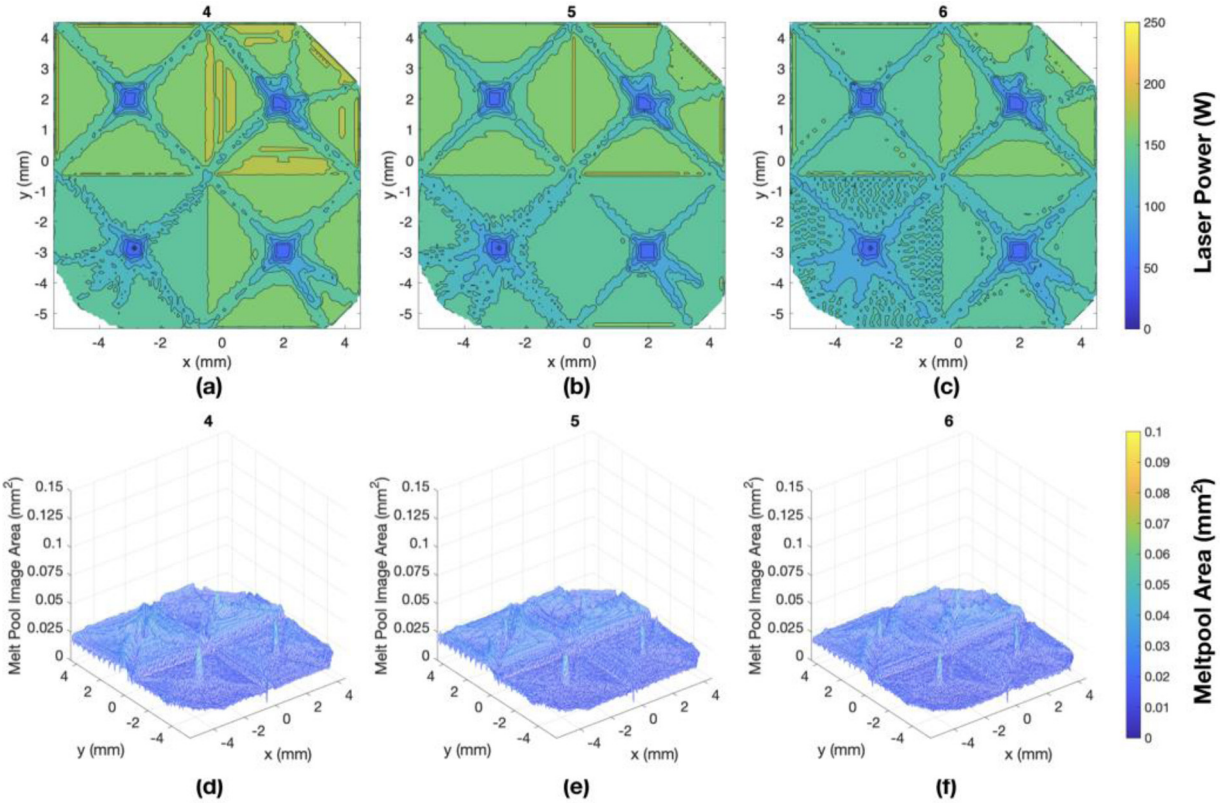

Fig. 9. Optimized laser power (a – c) and meltpool image area (d – f) for Scenarios 4 to 6.

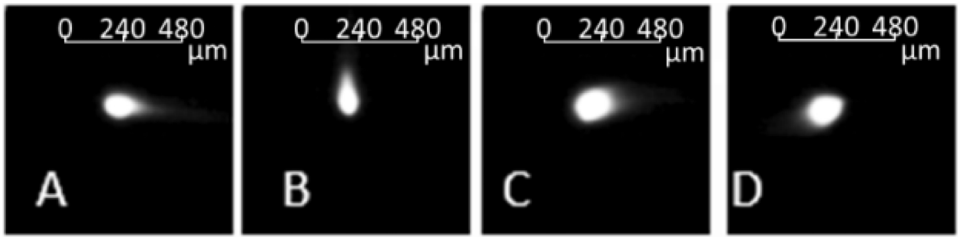

Fig. 10. Example meltpool images for Scenario 6.

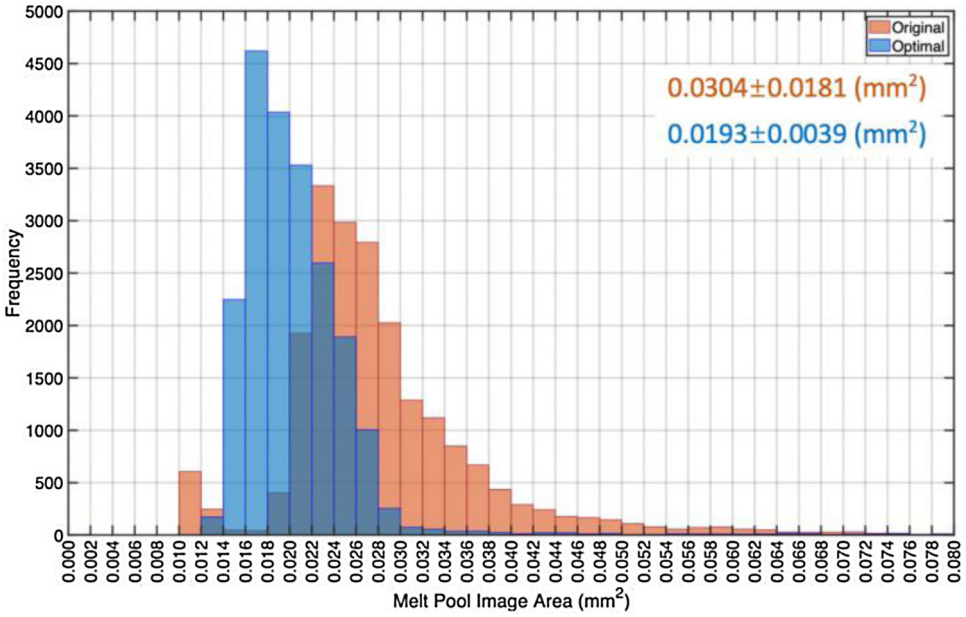

Fig. 11. Histogram for the original experiment (orange) and Experiment 6 (blue).

Table 4
Experimental results for original and optimized scan strategy.

Scenario	Mean ± SD (mm^2)	Objective (mm^2)
Original	0.0304 ± 0.0181	
1	0.0231 ± 0.0075	0.014 – 0.026
2	0.0221 ± 0.0073	0.016 – 0.024
3	0.0208 ± 0.0069	0.018 – 0.022
4	0.0208 ± 0.0044	0.014 – 0.026
5	0.0203 ± 0.0044	0.016 – 0.024
6	0.0193 ± 0.0039	0.018 – 0.022

value of c_2, which is coefficient for x_2 (laser power) in the polynomial, shows the dominant effect of laser power on the meltpool area. This justifies the using of laser power as the single design variable to reduce the meltpool variation.

$$\text{AREM} = \frac{1}{n}\left(\frac{\sum_{i=1}^{n} |y_i - \hat{y}_i|}{y_i}\right) y_i \neq 0 \tag{5}$$

Fig. 8 shows the optimized laser power distributions (a–c) and the resultant meltpool image areas (d–f) for Scenarios 1–3 (Table 2). The originally uniformly distributed laser power (Fig. 4b) was adjusted to the subject-specific conditions in Table 1, causing both the irregularities and peak values of the meltpool image area to be significantly reduced. The optimized scan strategy tends to reduce the laser power near the center and during the turns, when the energy density increases and/or residual heat accumulates. Scenario 3 has tighter objective meltpool area boundaries (Table 2) than Scenarios 2 and 1, therefore (c) reduces the laser power more aggressively than (b) and (a). However, due to the lower bound of the laser power being limited at 100 W for all three scenarios, none of them can completely remove the meltpool image area peak at the island center.

Scenarios 4–6 attempt to reach the objective meltpool area by extending the laser power constraints to 50 W–250 W (Table 2). The new optimized laser power distributions and the resultant meltpool image areas are shown in Fig. 9. The meltpool image area variation is further reduced, the peaks at the island center are almost leveled. Fig. 10 shows the example meltpool images at the same locations A – D as in Fig. 6, but for Scenario 6. Meltpool image area at location A and B remain similar in size as before but significantly reduced at C and D, compared with the original experiments (Fig. 7).

Fig. 11 compares the histogram of the meltpool image area of the original experiment and Scenario 6. The average meltpool image area in Scenario 6 is 0.0193 mm^2. The standard deviation is reduced from 0.0181 mm^2 to 0.0039 mm^2. Table 4 lists the averages and standard deviations for all experiments. The minimum standard deviation is achieved by Scenario 6. Both Scenarios 3 and 6 have the tightest area objectives, but Scenario 6 allows the power to be adjusted in a wider range. This demonstrated the effectiveness of this optimization method.

5. Summary and future work

There is an open field of research into laser scan strategy with the potential to reduce defects, control residual stress or microstructure, or improve the speed and efficiency of material consolidation. NIST AMMT provides control and monitoring capabilities for such research. This study demonstrated a meltpool prediction-based scan strategy, it maintained a more constant meltpool by adjusting laser power continuously based on the meltpool size predication made by the NBEM model. The variation of meltpool image area, measured by its standard

deviation, was reduced by 78 % over the constant power scan strategy (from 0.0181 mm^2 to 0.0039 mm^2). In a LPBF process the layer thickness is usually less than 100 μm, therefore many adjacent layers are sliced into the same geometry. The build environments, such as temperature and air flow rate, do not vary too much per layer neither. Therefore, the current layer meltpool images can be used to optimize the scan strategy for the next layer to achieve a layer-wise feedforward control.

The NBEM model simplifies the complicated thermal condition of a scan position into four NBEM factors, it is computationally effective but may also raise the modeling uncertainties due to the physical and numerical losses. To achieve a more comprehensive physical representation and real-time control, a deep learning approach can be used. The power, scan speed, and meltpool area plots in Fig. 3 can be superimposed into a multi-layer array to train a deep neural network model for regression or classification purposes. More specifically, the neural network regression model aims to capture more nonlinear features than the current polynomial approach to improve predictive accuracy. The optimization that builds upon a more accurate meltpool estimation can potentially provide more precise power adjustment. The deep neural network classification model, on the other hand, aims to identify whether the scan command needs to be adjusted. The superimposed array would construct the input layer. Power, speed, and meltpool area would be the three input nodes. The output layer has three nodes for power adjustment decisions. Increasing, maintaining, and decreasing the power would be three categories for the output. The neural network model would be trained to make a proper decision based on the original commands and optimized power adjustment. However, it requires more physical experiments for better training result. Current research of the author has designed an experiment with 12 unique scan patterns with different scan direction, island division, and power and speed settings [26]. The data can be potentially used to build the deep neural network model. This should provide a more accurate meltpool estimation at a faster processing time, and is believed to be the direction towards the real-time feedforward control of the AM process.

Authorship statement

All persons who meet authorship criteria are listed as authors, and all authors certify that they have participated sufficiently in the work to take public responsibility for the content, including participation in the concept, design, analysis, writing, or revision of the manuscript

Declaration of Competing Interest

The authors declare that there are no conflicts of interest.

References

[1] M. Mani, B. Lane, M.A. Donmez, S. Feng, S. Moylan, R. Fesperman, Measurement Science Needs for Real-time Control of Additive Manufacturing Powder Bed Fusion Processes, National Institute of Standards and Technology, Gaithersburg, MD, 2015.
[2] M. Grasso, B.M. Colosimo, Process defects and in situ monitoring methods in metal powder bed fusion: a review, Meas. Sci. Technol. 28 (2017) 044005.
[3] W.E. King, H.D. Barth, V.M. Castillo, G.F. Gallegos, J.W. Gibbs, D.E. Hahn, C. Kamath, A.M. Rubenchik, Observation of keyhole-mode laser melting in laser powder-bed fusion additive manufacturing, J. Mater. Process. Technol. 214 (2014) 2915–2925.
[4] H. Gong, K. Rafi, H. Gu, T. Starr, B. Stucker, Analysis of defect generation in Ti–6Al–4V parts made using powder bed fusion additive manufacturing processes, Addit. Manuf. 1–4 (2014) 87–98.
[5] L. Thijs, F. Verhaeghe, T. Craeghs, J.V. Humbeeck, J.-P. Kruth, A study of the microstructural evolution during selective laser melting of Ti–6Al–4V, Acta Mater. 58 (2010) 3303–3312.
[6] I. Yadroitsev, L. Thivillon, P. Bertrand, I. Smurov, Strategy of manufacturing components with designed internal structure by selective laser melting of metallic powder, Appl. Surf. Sci. 254 (2007) 980–983.
[7] S.A. Khairallah, A.T. Anderson, A. Rubenchik, W.E. King, Laser powder-bed fusion additive manufacturing: Physics of complex melt flow and formation mechanisms of pores, spatter, and denudation zones, Acta Mater. 108 (2016) 36–45.
[8] H. Yeung, B.M. Lane, M.A. Donmez, J.C. Fox, J. Neira, Implementation of advanced laser control strategies for powder bed fusion systems, 46th SME North Am. Manuf. Res. Conf. NAMRC 46 Tex. USA 26 (2018) 871–879.
[9] P.A. Hooper, Melt pool temperature and cooling rates in laser powder bed fusion, Addit. Manuf. 22 (2018) 548–559.
[10] H. Bikas, P. Stavropoulos, G. Chryssolouris, Additive manufacturing methods and modelling approaches: a critical review, Int. J. Adv. Manuf. Technol. 83 (2016) 389–405.
[11] A. Paul, M. Mozaffar, Z. Yang, W. Liao, A. Choudhary, J. Cao, A. Agrawal, A real-time iterative machine learning approach for temperature profile prediction in additive manufacturing processes, ArXiv190712953 Cs Stat (2019).
[12] Y. Zhang, G.S. Hong, D. Ye, K. Zhu, J.Y.H. Fuh, Extraction and evaluation of melt pool, plume and spatter information for powder-bed fusion AM process monitoring, Mater. Des. 156 (2018) 458–469.
[13] G. Tapia, S. Khairallah, M. Matthews, W.E. King, A. Elwany, Gaussian process-based surrogate modeling framework for process planning in laser powder-bed fusion additive manufacturing of 316L stainless steel, Int. J. Adv. Manuf. Technol. 94 (2018) 3591–3603.
[14] B. Zhang, S. Liu, Y.C. Shin, In-Process monitoring of porosity during laser additive manufacturing process, Addit. Manuf. 28 (2019) 497–505.
[15] M. Khanzadeh, S. Chowdhury, M. Marufuzzaman, M.A. Tschopp, L. Bian, Porosity prediction: supervised-learning of thermal history for direct laser deposition, Int. J. Ind. Manuf. Syst. Eng. 47 (2018) 69–82.
[16] L. Scime, J. Beuth, Anomaly detection and classification in a laser powder bed additive manufacturing process using a trained computer vision algorithm, Addit. Manuf. 19 (2018) 114–126.
[17] A. Nettekoven, S. Fish, U. Topcu, J. Beaman, Predictive iterative learning control with data-driven model for optimal laser power in selective laser sintering solid Free. fabr. Proc. 29th Annu. Int. *Solid Free*. Fabr. Symp. – Addit. Manuf. Conf. (2018).
[18] H. Yeung, J. Neira, B. Lane, J. Fox, F. Lopez, Laser path planning and power control strategies for powder bed fusion systems solid Free. fabr. Proc. 27th Annu. Int. Solid Free. Fabr. Symp. (2016).
[19] Lane, et al., Design, developments, and results from the NIST additive manufacturing metrology testbed (AMMT) solid Free. fabr. Proc. 26th Annu. Int. Solid Free. Fabr. Symp. (2016).
[21] L. Thijs, F. Verhaeghe, T. Craeghs, J.V. Humbeeck, J.-P. Kruth, A study of the microstructural evolution during selective laser melting of Ti–6Al–4V, Acta Mater. 58 (2010) 3303–3312.
[22] S. Clijsters, T. Craeghs, S. Buls, K. Kempen, J.-P. Kruth, In situ quality control of the selective laser melting process using a high-speed, real-time melt pool monitoring system, Int. J. Adv. Manuf. Technol. 75 (2014) 1089–1101.
[23] M. Rombouts, J.-P. Kruth, L. Froyen, P. Mercelis, Fundamentals of selective laser melting of alloyed steel powders, CIRP Ann.-Manuf. Technol. 55 (2006) 187–192.
[24] Z. Yang, Y. Lu, H. Yeung, S. Krishnamurty, From scan strategy to melt Pool prediction: a neighboring-effect modeling method, *Proc*. ASME 2019 Int. Des. Eng. Tech. Conf. Comput. Inf. Eng. Conf. 10 Anaheim CA USA ASME (2019).
[25] Z. Yang, D. Eddy, S. Krishnamurty, I. Grosse, P. Denno, F. Lopez, Investigating predictive metamodeling for additive manufacturing *ASME*, Int. Des. Eng. Tech. Conf. Comput. Inf. Eng. Conf. Pp V01AT02A020-V01AT02A020 Am. Soc. Mech. Eng. (2016).
[26] Brandon Lane, Ho Yeung, Process Monitoring Dataset from the Additive Manufacturing Metrology Testbed (AMMT): Three-Dimensional Scan Strategies, (2019).